

Article

Squaric Acid Core Substituted Unsymmetrical Squaraine Dyes for Dye-Sensitized Solar Cells: Effect of Electron Acceptors on Their Photovoltaic Performance

Safalmani Pradhan *, Yuki Kurokawa, Suraya Shaban  and Shyam S. Pandey * 

Graduate School of Life Science and Systems Engineering, Kyushu Institute of Technology, 2-4, Hibikino, Kitakyushu 808-0196, Japan; kurokawa.yuki207@mail.kyutech.jp (Y.K.); surayashaban@gmail.com (S.S.)

* Correspondence: pradhan.safalmani542@mail.kyutech.jp (S.P.); shyam@life.kyutech.ac.jp (S.S.P.)

Abstract: The design and development of sensitizing dyes possessing wide-wavelength photon harvesting encompassing visible to near-infrared (NIR) wavelength regions are unavoidable for increasing the overall efficiency of dye-sensitized solar cells (DSSCs). In this study, three far-red-sensitive squaraine sensitizers were designed computationally, synthesized, and characterized, aiming towards their suitability as a potential sensitizer for DSSCs. It has been found that the incorporation of an electron acceptor moiety in the central squaraine core brought about a red shift in the absorption maximum (λ_{\max}) and the emergence of a secondary absorption band in the blue region, thus broadening the photon-harvesting window. In addition, it also lowered the dye's HOMO energy level enabling a facile regeneration of the photo-excited dye, which improved the photovoltaic performance of SQ-223, exhibiting a photoconversion efficiency (PCE) of 4.67%. Thereafter, to address the issue of wide-wavelength photon harvesting, DSSCs were fabricated by co-adsorbing two complementary dyes SQ-223 and D-131 in various molar ratios. The DSSC fabricated with D-131 and SQ-223 in 9:1 molar ratio displayed the best photovoltaic performance with a PCE of 5.81%, a significantly higher PCE when compared to corresponding individual dye-based DSSCs containing D-131 (3.94%) and SQ-223 (4.67%).



Citation: Pradhan, S.; Kurokawa, Y.; Shaban, S.; Pandey, S.S. Squaric Acid Core Substituted Unsymmetrical Squaraine Dyes for Dye-Sensitized Solar Cells: Effect of Electron Acceptors on Their Photovoltaic Performance. *Colorants* **2023**, *2*, 654–673. <https://doi.org/10.3390/colorants2040034>

Academic Editor: Anthony Harriman

Received: 15 August 2023

Revised: 5 October 2023

Accepted: 17 October 2023

Published: 6 November 2023



Copyright: © 2023 by the authors. Licensee MDPI, Basel, Switzerland. This article is an open access article distributed under the terms and conditions of the Creative Commons Attribution (CC BY) license (<https://creativecommons.org/licenses/by/4.0/>).

Keywords: squaraine dyes; NIR sensitization; wide-wavelength photon harvesting; quantum chemical calculations; dye-sensitized solar cells

1. Introduction

Global population growth, contributing to a 1.3% yearly upsurge in energy demand, has increased energy consumption, depleting non-renewable resources, and causing adverse environmental consequences such as global warming and climate change [1,2]. This has motivated scientists to pursue clean alternative energy sources, with solar energy receiving substantial scientific interest due to its immense potential for meeting global energy requirements in an eco-friendly way [3]. In this context, photovoltaic technology can efficiently convert solar energy into electrical energy in a cost-effective manner [4]. Although the installation of silicon-based solar cells is rapidly growing, their relatively higher electricity production costs compared to fossil fuels have limited their large-scale implementation. As a result, third-generation solar cells, particularly dye-sensitized solar cells (DSSCs), have commanded significant attention owing to their inexpensive fabrication technique, the cheap and easy availability of resources, and their higher potential for harvesting photons, particularly in indoor settings [5]. The breakthrough research for harvesting this immensely available solar energy affordably was carried out by Gratzel and O'Reagan in 1991, where they reported an efficiency of 7.9% utilizing Ruthenium complex-based sensitizing dyes [6]. The use of natural dyes and pigments as sensitizers has also drawn particular attention from the scientific community towards DSSCs [7–9].

Furthermore, low-cost and sustainable DSSCs, coupled with green synthesis of sensitizers, hold huge potential for sustainable and cheaper solar energy solutions [10,11].

Dye-Sensitized Solar Cells (DSSCs) comprise a photoanode and photocathode, where a light-absorbing dye monolayer adsorbed onto a semiconductor like TiO₂ becomes photo-excited upon irradiation of light, injecting electrons into the semiconductor's conduction band (CB). The redox electrolyte sandwiched in between the two electrodes then regenerates the photo-excited dye; however, this regeneration process must be faster than the recombination process, thus necessitating a judicious design of the sensitizer which must possess a proper energetic balance with the semiconductor and the electrolyte [12–14]. According to earlier reports, a judiciously designed sensitizer resulted in a photoconversion efficiency (PCE) of 13.6% for D- π -A (Donor- π -Acceptor) dyes [15] and 12.5% for D-A- π -A dyes [16]. Organometallic dyes, mainly consisting of ruthenium-polypyridyl complexes [17,18] and zinc porphyrin dyes [19] and metal-free organic dyes [20,21] are the two classes of sensitizers utilized in DSSCs. Between the two classes of sensitizers, metal-free organic dyes command particular attention from researchers owing to their tunable energy levels, easy synthetic procedure, and comparatively lower toxicity, as the synthesis and purification of organometallic dyes are complex [22]. So far, the visible sensitizers utilized in DSSCs have exhibited high efficiency. But dyes like phthalocyanines [23,24], porphyrins [25,26], and polymethines [27], which are capable of harvesting near-infrared (NIR) photons, have commanded particular attention as they possess the ability to broaden the photon-harvesting window to further enhance PCE [28]. The metal-free polymethine class of dyes, particularly the squaraines, with their high molar extinction coefficient, tunable energetics, and effective absorption of light in the far-red to near-infrared (NIR) region, has garnered significant interest, primarily due to their intense absorption characteristics related to the D-A-D charge transfer interaction [29,30]. However, NIR dyes are known to have a smaller band gap [31], which makes the synthesis of efficient NIR sensitizers challenging. The D-A-D zwitterionic molecular framework-based squaraine dyes, which were first discovered by Triebs and Jacob in 1965, possess donor moieties on both sides of an electron-deficient squaric acid core (cyclobutene). The cyclobutene at the core functions as the acceptor unit [32]. Hence, the structure of these dyes allows for the logical incorporation of donor moieties on either side of the squaraine core along with the introduction of electron acceptors by nucleophilic substitution in the central squaraine core to facilitate the expansion of the light-harvesting window along with the tuning of the energy levels, i.e., highest occupied molecular orbital (HOMO) and lowest unoccupied molecular orbital (LUMO) [33,34]. In our previous research, we reported that only a substituent change while leaving the principal molecular framework unchanged can tune the energetics of the sensitizers by 0.1 eV [35].

Here, this study reports the theoretical design, synthesis, and photophysical, photovoltaic, and impedance characterization of three unsymmetrical squaraine sensitizers, SQ-220, SQ-222, and SQ-223, possessing intense optical absorption in the far-red region. In order to determine the sensitizers' theoretical energetics and theoretical electronic absorption spectra, theoretical calculations were carried out before their synthesis, utilizing the Gaussian16 program [36]. Based on earlier reports, the selection of the basis set and functional for the theoretical calculations was carried out [37]. The design of the dyes used in this study was based on the substitution of the central squaraine core with electron acceptors, a concept first put forward by Beverina et al. with respect to DSSC applications [38], which was necessary to lower the energy of the HOMO levels and control the energetics of the sensitizers in order to maintain their energetic cascade with mesoporous TiO₂ and redox electrolyte [35]. In addition to this, the central squaraine core was functionalized with the purpose of inducing the appearance of a secondary absorption peak within the visible spectrum that complements the primary absorption peak in the far-red region, thus effectively allowing the efficient capture of photons across a wide range of wavelengths [38]. In an interesting study, Wurthner et al. reported that squaraine dyes with central functionalization display a structurally rigid nature, where the central

cyclobutene ring constrains the π -backbone into a cisoid conformation [39]. According to Han et al., the elongated alkyl chains extending outward create a hydrophobic layer above the cis-configured dye monolayer on the surface of TiO_2 , a phenomenon that would hinder recombination [40]. Considering the above requirements, two-electron acceptors, namely, butyl cyanoacetate (SQ-222) [41] and 1,3-indandione (SQ-223) [42], were used in this work, and SQ-220 was used as a reference dye without any central substitution. Previous studies have highlighted the strong electron-accepting capability of butyl cyanoacetate, but it is worth mentioning here that 1,3-indandione exhibits an even more pronounced electron-accepting ability in comparison [43,44]. The light absorption window broadened as a consequence of incorporating electron acceptors in the molecular framework, and the absorption maximum (λ_{max}) also shifted to higher wavelengths [33,45]. In addition to this, the best-performing dye, SQ-223, was also utilized together with a visible dye, D-131, in order to co-sensitize the mesoporous TiO_2 with the aim of increasing PCE further [46]. Therefore, three far-red-sensitive sensitizers with different electron acceptors, as shown in Figure 1, were synthesized and their effect on the energetics, along with their photophysical and photovoltaic characteristics, were comprehensively studied.

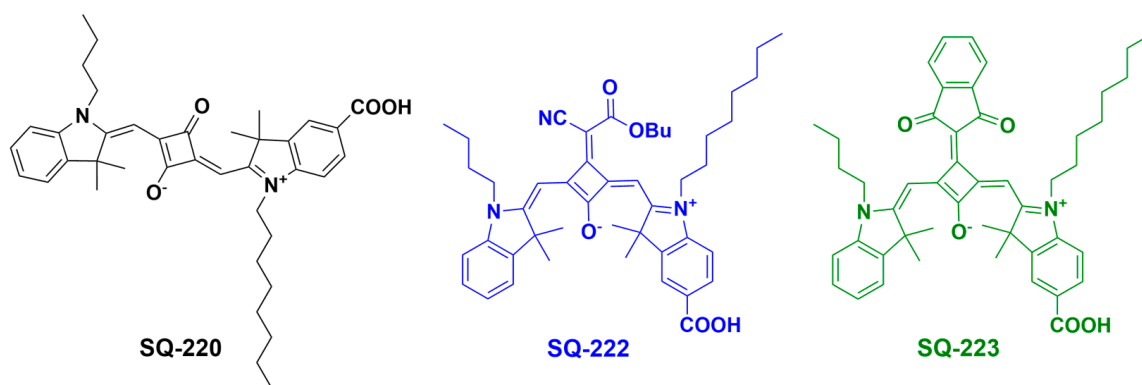


Figure 1. Structures of far-red-sensitive squaraine sensitizers.

2. Experimental

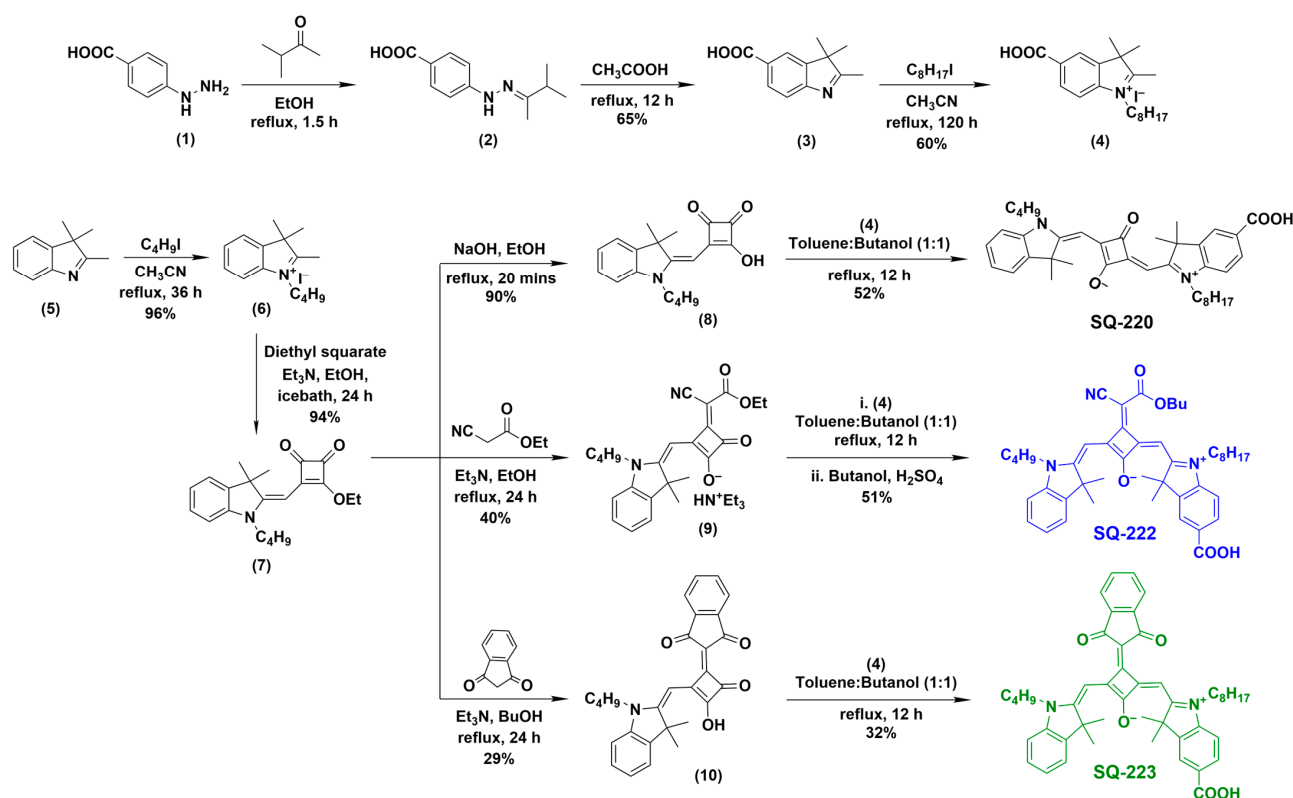
2.1. Materials and Methods

All of the chemicals and solvents utilized in this investigation were of analytical/spectroscopic grade; hence, no additional purification was carried out. The structural identities of the sensitizers and their corresponding intermediates were proven by the use of fast atom bombardment mass spectrometry (FAB-MS). Further, the nuclear magnetic resonance (NMR) spectra of the sensitizers in chloroform- d_6 (CDCl_3) were measured by an NMR spectrometer (JEOL, 500 MHz) for confirmation of their structure. An ultraviolet (UV)-visible-near-infrared (NIR) spectrophotometer (JASCO model V550) was utilized to measure the sensitizers' absorption spectra in the solid as well as the solution (ethanol) state. In the solid state, the absorption spectra were measured by adsorbing the respective sensitizers onto a transparent TiO_2 layer of 5 μm thickness. The sensitizers' energy band diagrams were constructed by initially estimating their HOMO energy level utilizing cyclic voltammetry (CV), then estimating their band gap energy (E_g) with the help of a relationship $E_g = 1240/\lambda_{\text{opt}}$, in which λ_{opt} , determined from the sensitizers' solid-state absorption spectra, represents the optical absorption edge. Finally, the equation $\text{LUMO} = \text{HOMO} + E_g$ was utilized to measure the energy of the LUMO. The CV of the sensitizers, recorded using an automatic polarization system (HSV-100, Hakuto Denko, Japan), was utilized to estimate the sensitizers' HOMO energy level. An electrochemical cell with three electrodes, viz., Platinum (Pt) wire (working electrode), Pt foil (counter electrode), and Ag/AgCl (reference electrode), was utilized for recording the sensitizers' CV. The CV of the sensitizers was measured at a scan rate of 50 mV/s, using a dye solution (2 mM) along with tetrabutylammonium hexafluorophosphate (0.4 M) in dimethyl formamide (DMF). Prior to this,

the CV of the reference redox material, i.e., ferrocene (Fc), was recorded. The shift of the first oxidation potential of each sensitizer with respect to the oxidation potential of the Fc^+/Fc redox couple was utilized to determine the energy of the HOMO of the sensitizers. The energy of the HOMO level of the Fc^+/Fc redox couple was taken to be -5.08 eV, an experimentally calculated value reported by Su and Girault [47]. The sensitizers' emission spectra were recorded utilizing a fluorescence spectrometer (JASCO FP-6600). A frequency range of 10^{-1} to 10^5 Hz and a signal amplitude of 10 mV were used for Electrochemical Impedance Spectroscopy (EIS) measurements. For the optimization of molecular structure, estimation of energy of the HOMO and the LUMO, and determination of the theoretical absorption spectra, theoretical quantum chemical calculations were conducted utilizing the Gaussian16 program on a multiprocessor Dell workstation [36]. Employing ethanol as the solvent, the calculations were carried out for a single, isolated molecule utilizing the polarization continuum model (PCM), time-dependent density functional theory (TD-DFT), 6-311G basis set, and B3PW91 hybrid functional [37].

2.2. Synthesis of Far-Red-Sensitive Unsymmetrical Squaraine Sensitizers

The squaraine sensitizers utilized in this investigation were synthesized in accordance with the synthetic scheme shown in Scheme 1. (Refer to supplementary material, Section S1, Scheme S1, for a detailed synthetic procedure.)



Scheme 1. Scheme of synthesis for the far-red-sensitive unsymmetrical squaraine sensitizers. (1) 4-hydrazinobenzoic acid; (2) 4-[(1,2-Dimethylpropylidene)hydrazinyl]benzoic acid; (3) 2,3,3-trimethyl-3H-indole-5-carboxylic acid; (4) 5-carboxy-2,3,3-trimethyl-1-octyl-3H-indolium iodide; (5) 2,3,3-trimethyl-3H-indole; (6) 1-butyl-2,3,3-trimethyl-3H-indol-1-ium iodide; (7) (E)-3-((1-butyl-3,3-dimethylindolin-2-ylidene)methyl)-4-ethoxycyclobut-3-ene-1,2-dione; (8) (E)-3-((1-butyl-3,3-dimethylindolin-2-ylidene)methyl)-4-hydroxycyclobut-3-ene-1,2-dione; (9) (Z)-2-(((E)-1-butyl-3,3-dimethylindolin-2-ylidene)methyl)-3-(1-cyano-2-ethoxy-2-oxoethylidene)-4-oxocyclobut-1-en-1-olate triethylammonium (10) (E)-2-((1-butyl-3,3-dimethylindolin-2-ylidene)methyl)-3-(1,3-dioxo-1,3-dihydro-2H-inden-2-ylidene)-4-oxocyclobut-1-en-1-olate.

2.3. Fabrication of DSSCs

DSSCs were fabricated utilizing a fluorine-doped tin oxide (FTO)-coated transparent conducting glass. In order to fabricate the photoanode (working electrode), FTO-coated glass was cut into (2×2.5) cm² area, washed under sonication for 10 min each in detergent water, distilled water, acetone, and isopropanol (IPA), followed by exposure to UV-ozone (30 min). After this, the UV-ozone-treated substrates were screen printed first with Ti-nanoxide (T/SP), and then with Ti-nanoxide (D/SP) to create a 12 μ m thick double layered TiO₂. The active area of the double-layered TiO₂ was kept precisely at 0.25 cm² using a metal mask. After screen printing each layer, the substrates were baked in a muffle furnace for 45 min at 450 °C. The TiO₂-coated substrates were dipped in an aqueous TiCl₄ solution (40 mM) for one hour at a temperature of 70 °C to perform the surface treatment. Following this, the dye adsorption was conducted by dipping the surface-treated TiO₂ substrates in the sensitizers' ethanolic solution (0.2 mM), also consisting of chenodeoxycholic acid (CDCA) (20 mM), for 4 h under room temperature conditions. To prepare the photocathode (counter electrode), pre-drilled FTO glass substrates of the same dimensions were cleaned in a similar way as the photoanode and subjected to spin-coating using Platisol-T (Solaronix) solution to obtain an ultrathin layer of Pt as the catalytic layer. Following this, the photoanode and the photocathode were affixed together at 110 °C utilizing a hot melt spacer (Solaronix Meltonix) of 60 μ m thickness. As a final step of device fabrication, the redox electrolyte (iodide/triiodide, I⁻/I₃⁻) was injected via a pre-drilled hole in the photocathode. To prevent leakage of the electrolyte, UV-curable resin (Three-bond, Japan) was used to seal the holes. The redox electrolyte (I⁻/I₃⁻) comprised 0.05 M Iodine (I₂), 0.1 M Lithium Iodide (LiI), 0.5 M t-butyl pyridine (TBP), and 0.6 M 1,2-dimethyl-3-propyl imidazolium iodide (DMPII) in anhydrous acetonitrile as solvent. A solar simulator (CEP-2000 Bunko Keiki Co., Ltd., Tokyo, Japan) fitted with a Xenon lamp (Bunko Keiki BSO-X150LC) was utilized to characterize the photovoltaic performance of the fabricated DSSCs under a simulated solar irradiation of 100 mW/cm².

3. Results and Discussion

3.1. Optical Characterization

The sensitizers' UV-visible spectra recorded both in solution and solid state, along with their fluorescence emission spectra, are depicted in Figure 2. Furthermore, the optical parameters deduced therefrom are tabulated in Table 1. The dyes exhibit typical squaraine dye characteristics by showing sharp and intense light absorption along with slightly blue-shifted vibronic shoulders, principally in the spectrum's far-red region (500–700 nm). This intense light absorption is primarily due to electronic transition (π - π^*), i.e., HOMO to LUMO electronic transition of the dye. The formation of H-aggregates in solution has been considered to be the reason behind the appearance of vibronic shoulders in their absorption spectrum, which intensifies on TiO₂'s surface (solid state) because of enhanced intermolecular interactions. In addition to this intense peak in the far-red region, SQ-222 exhibits absorption peaks of comparatively lower intensities at 416 and 392 nm, related to HOMO-1 \rightarrow LUMO and HOMO \rightarrow LUMO+1 electronic transitions, respectively. Similarly, SQ-223 exhibits an absorption peak of lesser intensity in the blue region at 458 nm, related to HOMO \rightarrow LUMO+2 electronic transition. It is worth mentioning that the theoretical absorption spectra for SQ-222 also exhibit three permitted transitions at 616, 411, and 404 nm, related to HOMO \rightarrow LUMO, HOMO-1 \rightarrow LUMO, and HOMO \rightarrow LUMO+1 electronic transition, respectively. Similarly, the theoretical absorption spectra of SQ-223 also show two permitted transitions at 617 and 466 nm, related to HOMO \rightarrow LUMO and HOMO \rightarrow LUMO+2 electronic transition, respectively, thus establishing an excellent correlation between the experimental and theoretical results. (Refer to Section S2, Figure S1, Table S1 for more details.) The molar extinction coefficients (ϵ) between 1.12×10^5 to 3.08×10^5 dm³ mol⁻¹ cm⁻¹ for these sensitizers are comparable to the ϵ value (1.6 – 3.2×10^5 dm³ mol⁻¹ cm⁻¹) of squaraine dyes reported in the literature [48,49]. This is another typical squaraine dye characteristic exhibited by these sensitizers. Their molar extinction coefficients are almost

three times greater than that of a well-known visible sensitizer D-131 ($0.46 \times 10^5 \text{ dm}^3 \text{ mol}^{-1} \text{ cm}^{-1}$), and approximately ten times higher than that of N3 ($0.14 \times 10^5 \text{ dm}^3 \text{ mol}^{-1} \text{ cm}^{-1}$) [50]. The high ϵ values primarily result from the intramolecularly delocalized transfer of charges originating from the HOMO (indole group) to the LUMO (cyclobutene or squaraine core), aided by extended π -conjugation and molecular planarity [29]. Additionally, the high ϵ values also result from the presence of notable electron density on the cyclobutene ring of the central core [51]. The inset in Figure 2a reveals that, apart from SQ-220, the other two dyes exhibit bathochromically shifted absorption maxima (λ_{max}), primarily attributable to the elongation of π -conjugation as a consequence of the incorporation of electron acceptors in the squaraine core [33].

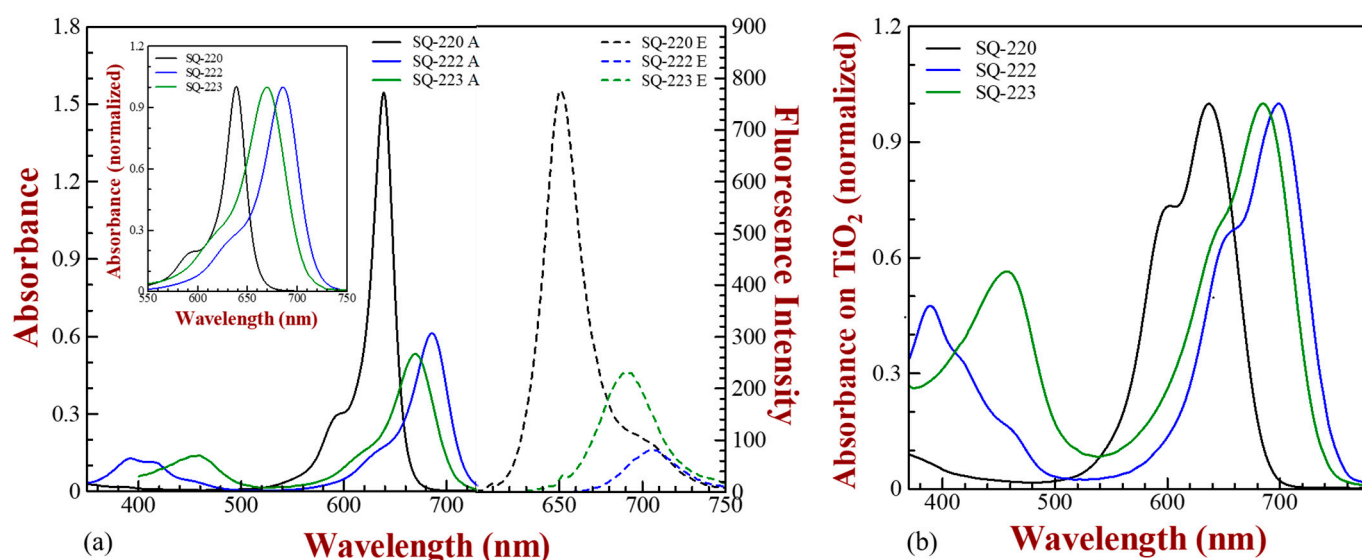


Figure 2. (a) UV-visible absorption, normalized absorption (in the inset) and fluorescence emission spectra of 5 μM ethanolic dye solutions; (b) Normalized UV-visible spectra of the sensitizers adsorbed on transparent TiO_2 of 5 μm thickness (solid state).

Table 1. Optical parameters deduced for the squaraine sensitizers from their UV-visible absorption and fluorescence emission spectra in the solution state as well as the solid state.

Sensitizing Dye	$\epsilon^{(i)}$ ($\text{dm}^3 \text{ mol}^{-1} \text{ cm}^{-1}$)	$\lambda_{\text{max}}(\text{Abs})^{(ii)}$ (Solution)	$\lambda_{\text{max}}(\text{Em})^{(iii)}$	Stokes Shift ^(iv)	$\lambda_{\text{max}}^{(v)}$ (Solid-State)	$\lambda_{\text{opt}}^{(vi)}$	Band Gap (E_g) ^(vii) (eV)	Extent of Aggregation
SQ-220	3.08×10^5	638 nm	650 nm	12 nm	636 nm	686 nm	1.81	0.73
SQ-222	1.22×10^5	686 nm	707 nm	21 nm	699 nm	752 nm	1.65	0.69
SQ-223	1.12×10^5	670 nm	692 nm	22 nm	685 nm	740 nm	1.68	0.66

(i) Molar extinction coefficient of the sensitizers; (ii) absorption maxima of the sensitizers; (iii) emission maxima of the sensitizers; (iv) Stokes shift, a shift of the emission maxima with respect to the absorption maxima; (v) solid-state absorption maxima, (vi) optical absorption edge (λ_{opt}), i.e., the onset wavelength in the sensitizers' solid-state absorption spectra; (vii) band gap (E_g), given by the equation $E_g = 1240/\lambda_{\text{opt}}$.

For a more precise understanding of the dye aggregation behavior, solid-state absorption spectra of the sensitizers adsorbed upon transparent TiO_2 of 5 μm thickness were recorded. Figure 2b shows the sensitizers' normalized solid-state absorption spectra. Compared to the solution-state absorption spectra, Figure 2b shows a marked increase in the intensity of the vibronic shoulder around 600–650 nm, mainly due to H-aggregate formation [52]. Moreover, these dyes exhibit spectral broadening, particularly when adsorbed onto TiO_2 (solid-state), as evident from Figure 2b. Specifically, in the case of SQ-222 and SQ-223, an intensification of the absorption peak in the blue region occurs, which contributes to an enhanced capability of absorbing light in the broad wavelength region. The higher

dye aggregation on the TiO_2 surface caused by their interaction with TiO_2 via the ester bonds following the deprotonation of the carboxylic acid is the main reason for the spectral broadening that has been seen in the solid state [53]. Furthermore, in the lower wavelength region of the spectrum, a higher extent of spectral broadening is observed, which has mostly been attributed to the H-aggregation of dye molecules on the TiO_2 surface [54]. Zhang et al. has shown that the formation of H-aggregates hinders injection of electrons into the TiO_2 's CB from the dye's LUMO, thus hampering the photovoltaic performance [55]. Therefore, earlier reports have demonstrated that using an anti-aggregation agent, particularly CDCA, suppresses aggregate formation [56]. During the fabrication of DSSCs, the CDCA concentration was adjusted based on the extent of aggregation (Table 1), given by the quotient of the H-aggregate band's (vibronic shoulder) absorbance value to the monomer band's absorbance value in the solid state. In addition to this, the CDCA concentration (20 mM) was optimized by fabricating DSSCs using various CDCA concentrations (10, 20, and 30 mM). The sensitizers' emission spectra are displayed in Figure 2a. Along with narrow spectral width, Figure 2a shows a bathochromically shifted emission maximum with the offset extending until 730 nm. The value of Stokes shift, basically a shift of the emission maxima with respect to the absorption maxima, is summarized in Table 1. Since the dyes under study exhibit much lower Stokes shift values, it can be concluded that their conformational stability is maintained even in the excited state [57]. Their Stokes shift values are far lower than that of the standard visible sensitizers normally used in DSSC research.

3.2. Electrochemical Characterization

With two oxidation peaks and one reduction peak, squaraine dyes display strong electrochemical activity and prominent redox behavior. The extraordinarily high electrochemical stability of these dyes has been proven; even after 3500 continuous redox cycles, essentially no alteration in the shape or location of the redox peaks was observed [49]. CV has been commonly utilized to measure the energy of the HOMO of the sensitizing dyes. Section S3, Figure S2 (see supplementary material) shows the CV of the DMF solution of the sensitizing dyes as well as that of a standard reference material, Fc, also in DMF. The CV was recorded under same electrochemical conditions as discussed earlier. All the dyes used in this study exhibit characteristic squaraine behavior with two oxidation peaks and one reduction peak in the potential range between 0.5 V and 1.4 V, along with an irreversible reduction peak in the potential range between -0.6 V and 0 V attributable to virtual redox states. The shift of the sensitizing dye's first oxidation peak relative to the Fc^+/Fc 's oxidation peak, was determined in order to estimate the energy of the HOMO of the sensitizing dyes. A closer analysis of Figure S2 shows that the introduction of electron acceptors, butyl cyanoacetate, and 1,3-indandione, respectively, in the squaraine core of SQ-222, and SQ-223, caused the first oxidation peak to shift towards higher potential, thereby also leading to a lowering of HOMO energy levels. The lowering of the HOMO energy level of these dyes is related to the stabilization of molecular orbitals on introducing electron acceptors into the molecular framework. SQ-223, substituted with the strongest electron acceptor among the two [43,44], exhibited the largest shift of the first oxidation peak relative to Fc, thereby also exhibiting the lowest energy of the HOMO. Finally, energy band diagram was made using the CV estimated energy of the HOMO, the value of band gap energy (E_g) estimated from the dye's solid-state absorption spectra, and the energy of the LUMO determined using the relationship $\text{LUMO} = \text{HOMO} + E_g$.

3.3. Energy Band Diagram

For a DSSC's efficient functioning, the sensitizing dyes should have a suitable energy matching with respect to the semiconductor and the redox electrolyte, which are TiO_2 and I^-/I_3^- , respectively, in the present work. The facile injection of electrons and the easy regeneration of the dye are the most significant aspects of efficient device functioning. However, a facile electron injection occurs only when the CB of TiO_2 possesses a lower

energy than the dye's LUMO. Similarly, efficient dye regeneration occurs only when the dye's HOMO lies at a lower energy level than the redox potential of the electrolyte. The energy band diagram in Figure 3 was then created using I^-/I_3^- redox electrolyte, whose redox potential was assumed to be -4.9 eV relative to vacuum or 0.44 V vs. NHE, and TiO_2 , whose CB energy level was considered to be -4.0 eV taking into consideration the most negative quasi-Fermi level correlating to the TiO_2 's flat band potential (0.7 V vs. SCE) [58,59]. As shown in Figure 3, a good energetic matching between the sensitizing dyes, mesoporous TiO_2 , and the redox electrolyte allows for an efficient injection of electrons and also efficient regeneration of the photo-excited sensitizer.

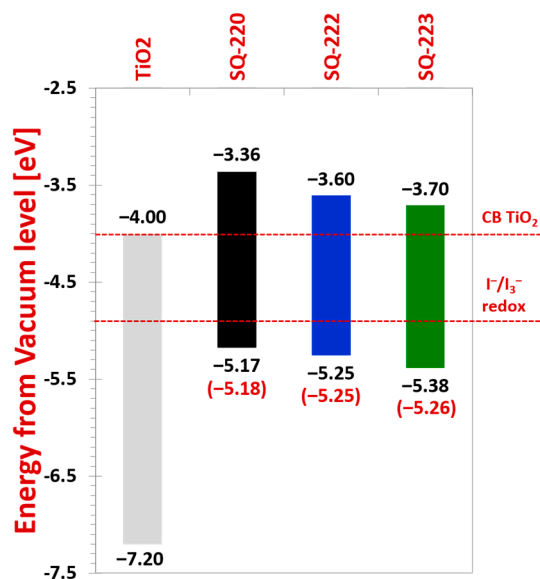


Figure 3. Energy band diagram for the sensitizers. (The HOMO energy level's theoretically calculated values are given in parentheses).

The perusal of Figure 3 shows that the fine-tuning of the sensitizers' energetics with respect to the semi-conductor and the redox electrolyte by the introduction of electron acceptors in the central core has led to facile injection of electrons and easy regeneration of the dye, thus resulting in minimum energy losses [60]. Also, upon a closer analysis of Figure 3, it becomes evident that the observed red shift in λ_{max} of SQ-222 and SQ-223 (Figure 2a) due to the extension in π -conjugation correlates with a corresponding decrease in the band gap energy, hence leading to hampered electron injection. The low-lying HOMO energy levels of SQ-222 and SQ-223 facilitated efficient dye regeneration, even though facile electron injection was compromised. Among the three sensitizing dyes under study, SQ-220, with the highest-lying LUMO, provides an energy barrier of 0.64 eV for injection of electrons. In contrast to this, SQ-223 has the lowest-lying LUMO, thus providing an energy barrier of 0.30 eV for injection of electrons. A high energy barrier, as in the case of SQ-220, is highly desirable, as it favors the process of electron injection more than recombination, i.e., electron back-transfer process, either to the dye's HOMO or to the redox electrolyte. Hence, SQ-223 has a slightly hampered electron injection compared to the other sensitizers. However, it is expected to have the most efficient dye regeneration owing to it having the lowest value of HOMO energy level. As discussed earlier, the introduction of electron acceptors in the molecular framework has resulted in a downward shift of the HOMO energy level. SQ-223, possessing the strongest electron acceptor, 1,3-indandione, exhibited the lowest HOMO energy level, mainly credited to the stabilization of molecular orbitals on introducing electron acceptors. Butyl cyanoacetate, with its relatively lesser electron-accepting ability, exhibited a dye regeneration energy barrier of 0.35 eV. SQ-220, with no electron acceptor in its molecular framework, exhibited the highest energy of the

HOMO level, thus resulting in a dye regeneration energy barrier of only 0.27 eV, leading to a less efficient dye regeneration.

3.4. Quantum Chemical Calculations

Quantum chemical calculations using density functional theory (DFT) are extensively utilized for designing and developing novel sensitizers. These calculations provide prior knowledge about the energetics, absorption spectra, and electron density distribution in both the HOMO and the LUMO of the sensitizer to assess their suitability as a sensitizer [61]. The computational cost is largely decreased by employing the Hartree–Fock method in DFT and taking into account a lone pair electronic correlation. According to previous reports, employing the time-dependent extension of DFT, or TD-DFT, together with a correlation functional led to a more accurate match between the theoretical electronic absorption spectrum and its experimental data counterpart [62]. For optimizing the structure of the sensitizers, theoretical calculations were carried out with the help of the Gaussian16 program, utilizing DFT, 6-311G basis set, B3PW91 hybrid functional, and employing PCM with ethanol as solvent. The accuracy of the theoretical calculations can be validated by a perusal of Figure 3, which reveals a good match between the energy of the HOMO estimated theoretically and the energy value calculated experimentally. The electron density distribution in the HOMO and the LUMO of the sensitizing dyes along with their optimized structure are shown in Figure 4.

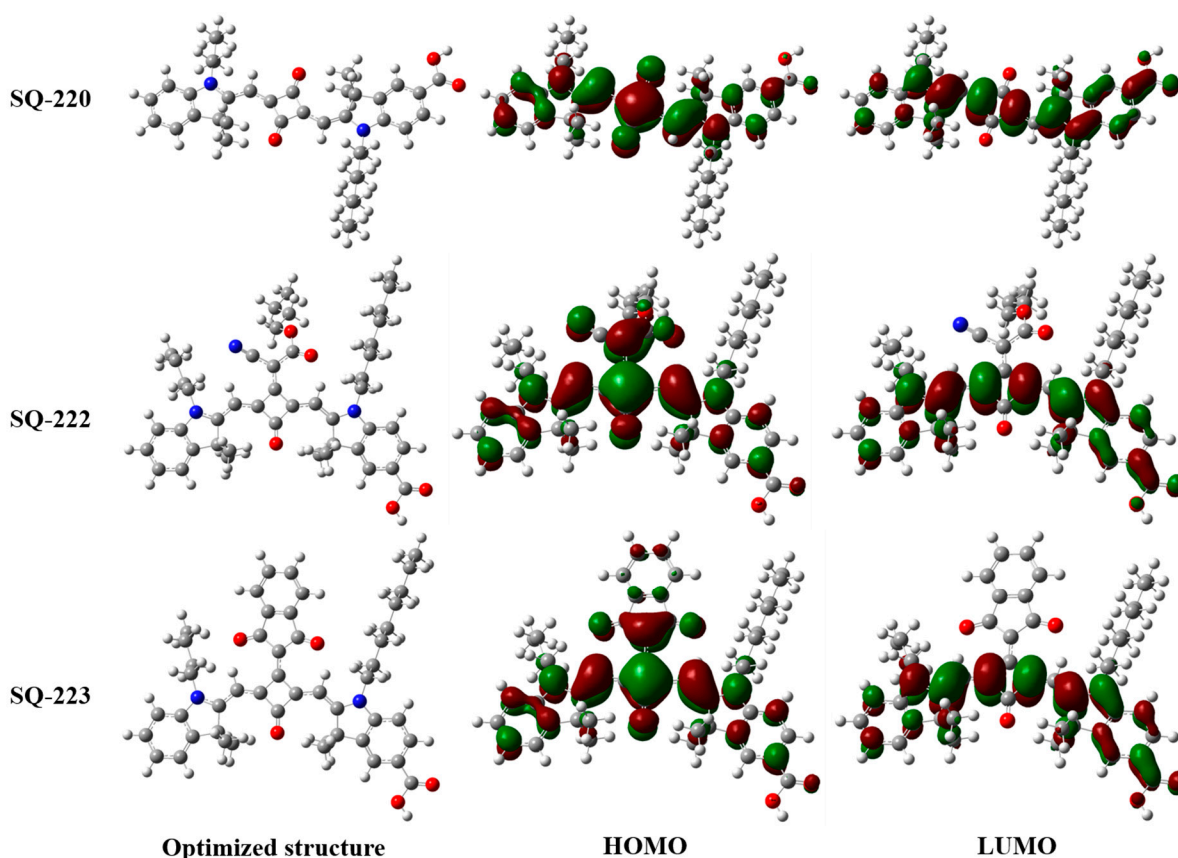


Figure 4. Optimized structure and the HOMO and LUMO electron density distribution.

As is evident from Figure 4, the electron density distribution in the dye's HOMO is primarily present in the cyclobutene ring at the center with minor extensions towards the donor groups attached on either sides and also towards the electron acceptors, in SQ-222 and SQ-223. However, the electron density in the dye's LUMO is sufficiently diverted away from the central cyclobutene ring towards the carboxylic acid, thus showing the

feasibility of intramolecular charge transfer (ICT) and charge separation on excitation. SQ-220, with no central substitution, exhibits the highest electron density diversion towards the carboxylic acid. The carboxylic acid in the LUMO consists of high electron density, thus ensuring a good electronic coupling between the TiO₂'s unoccupied d-orbitals and the excited sensitizer. This then allows for efficient injection of electrons into TiO₂'s CB. However, the low-lying LUMO level of SQ-223 could lead to slightly impeded electron injection, even though it exhibits a high electron density in carboxylic acid.

3.5. Photovoltaic Characterizations

The high molar extinction coefficients, NIR absorption, appropriate anchoring group, and a good energetic cascade of the sensitizer with the semiconductor and the electrolyte justified the use of these sensitizers as photon harvesters in DSSCs. Therefore, photovoltaic characterizations were carried out using these sensitizers under simulated solar irradiation of 100 mW/cm² in order to investigate the potential of these sensitizers as photon harvesters in DSSCs, as well as the influence of electron acceptors on their photovoltaic performance. DSSCs were fabricated utilizing the sensitizers, under identical experimental conditions such as concentration of the sensitizing dye (0.2 mM), CDCA (20 mM), and dipping time (4 h). At the same time, other device components, such as the composition of the photoanode, counter electrode (Pt), and redox electrolyte (I⁻/I₃⁻), were kept identical. Figure 5 displays the photovoltaic characteristics of fabricated DSSCs using various sensitizers, as well as the photocurrent action spectrum following illumination with monochromatic light.

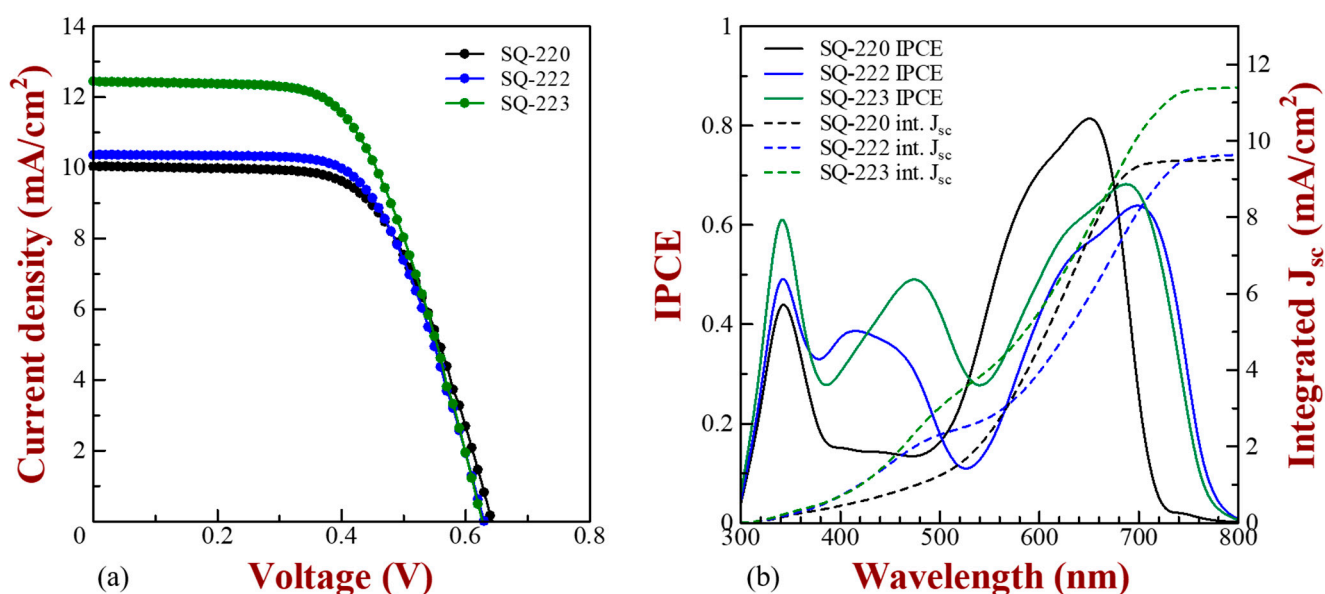


Figure 5. (a) Photovoltaic characteristics of fabricated DSSCs using dyes SQ-220, SQ-222, and SQ-223, under a simulated solar irradiation of 100 mW/cm²; (b) Photocurrent action spectra of the same DSSCs after illumination with monochromatic light.

The photovoltaic characteristics of the fabricated DSSCs, including their short-circuit current density (J_{sc}), open-circuit voltage (V_{oc}), fill factor (FF), and overall PCE (%), are summarized in Table 2. The dye loading amounts on the mesoporous TiO₂ after 4 h of dipping the substrates in the respective dye solutions has also been tabulated in Table 2. As evident in Figure 5 and Table 2, with a J_{sc} of 10.04 mA/cm², V_{oc} of 0.65, and FF of 0.62, SQ-220 with no central functionalization exhibited an overall PCE of 4.02%, which was slightly lower than the PCE (4.5%) obtained by Yum et al. for a dye with similar molecular framework [53]. The low FF value as a result of higher FTO resistance of 23 Ω /cm² (when compared to a resistance of 15 Ω /cm² for the FTO substrate used by Yum et al.) for the DSSCs fabricated in this work might be the reason for this observed

difference [56]. Similarly, SQ-222, consisting of butyl cyanoacetate as an electron acceptor in the squaraine core, exhibited an efficiency of 4.12%, which was slightly lower than the PCE (4.6%) obtained by Qin et al. using a dye with similar molecular framework with ethyl cyanoacetate as an electron acceptor [40]. This slightly lower value may be attributed to the inability of the shorter butyl chain to prevent recombination effectively [63]. Finally, with a J_{sc} of 12.4 mA/cm², V_{oc} of 0.63, and FF of 0.60, SQ-223, possessing the 1,3-indandione moiety as an electron acceptor, showed the best photovoltaic performance, yielding an overall PCE of 4.67%. An excellent photon harvesting, principally in the solar spectrum's far-red to NIR region, as well as partial photon harvesting in the visible region, contributed to the DSSC fabricated with SQ-223 achieving the highest J_{sc} of 12.4 mA/cm². SQ-223 exhibited a better photovoltaic performance despite having the lowest energy barrier (0.30 eV) for the injection of electrons and comparatively less electronic coupling at the anchoring group than SQ-220. This is mainly due to the easy regeneration of the photo-excited dye, in the case of SQ-223, facilitated by the low-lying HOMO energy level as well as wide-wavelength photon harvesting. Even though SQ-220 has an incident photon-to-current conversion efficiency (IPCE) of 80%, compared to 64% IPCE of SQ-222, the two sensitizers exhibit similar values of J_{sc} . This may be explained by the fact that even though SQ-222 possess only 64% IPCE, it has a photon-harvesting window that extends to almost 800 nm (as in SQ-223) and also harvests photons slightly in the visible region (400 nm–500 nm), although its photon harvesting in this region is lower than that of SQ-223. However, SQ-220 harvests photons only up to 720 nm and does not absorb in the visible region. Even though SQ-220 has a higher energy barrier (0.64 eV) for injection of electrons, as shown in Figure 3, and also demonstrates a strong electronic coupling because of the presence of significant electron density in the carboxylic acid, as shown in Figure 4, it was unable to outperform SQ-222 and SQ-223, mainly because SQ-220 has an energy barrier of only 0.27 eV for the dye regeneration along with a relatively narrow photon-harvesting window. The higher J_{sc} and hence PCE of SQ-223, as compared to SQ-222, may be a result of slightly higher photon harvesting by SQ-223 both in the visible region and NIR region. In addition to this, SQ-223 possesses a dye regeneration energy barrier of 0.48 eV, resulting in an efficient regeneration of the dye. The higher PCE of SQ-223 is thus credited to its wider photon-harvesting window, an adequate driving force for dye regeneration, minimum aggregation, and a reasonable driving force (0.30 eV) for electron injection. SQ-223 exhibits the highest dye loading and SQ-222 shows the lowest dye loading among the sensitizing dyes utilized in this study, as evident from Table 2. A closer look at the parameters summarized in Table 2 reveals that the amount of dye loaded onto the semiconductor (TiO₂) directly influences the photovoltaic performance, with SQ-223 exhibiting the best photovoltaic performance. Although SQ-220 exhibits a higher dye loading amount than SQ-222, it could not outperform SQ-222, mainly due to its lower dye regeneration ability and narrow photon-harvesting window.

Table 2. Photovoltaic parameters deduced after photovoltaic characterizations of DSSCs.

Sensitizing Dye	J_{sc} [mA/cm ²]	Integrated J_{sc} [mA/cm ²] (% Deviation)	V_{oc} [V]	FF	PCE [%]	Dye Loading [nmol cm ⁻² μm ⁻¹]
SQ-220	10.04 (9.93 ± 0.23)	9.49 (5.49)	0.65 (0.64 ± 0.02)	0.62 (0.63 ± 0.01)	4.02 (4.02 ± 0.03)	1.02
SQ-222	10.36 (10.25 ± 0.19)	9.63 (7.05)	0.64 (0.63 ± 0.01)	0.62 (0.61 ± 0.01)	4.12 (3.94 ± 0.15)	0.47
SQ-223	12.44 (11.93 ± 0.46)	11.40 (8.36)	0.63 (0.62 ± 0.01)	0.60 (0.60 ± 0.01)	4.67 (4.42 ± 0.18)	1.25

The mean values of different parameters of four individual DSSCs are presented in parentheses along with their standard deviations. The values shown above the parentheses in each case demonstrate the best cell parameters.

3.6. Electrochemical Impedance Spectroscopy (EIS)

EIS is a vital technique for examining the charge transport characteristics of a typical DSSC. Hence, it has been utilized for the characterization of the DSSCs fabricated utilizing the sensitizers under investigation, in order to understand the implication of internal resistance, interfacial properties, and charge transfer/transport processes on the photovoltaic performance of the DSSCs. The EIS analysis was conducted under a constant light illumination (100 mW/cm^2) by biasing the DSSCs at open-circuit conditions. As discussed in the previous section, despite exhibiting the best overall PCE, SQ-223 exhibited a slightly lower V_{oc} (0.63 V) than the V_{oc} exhibited by SQ-220 and SQ-222. To explain this anomaly, analysis of the Nyquist plot in Figure 6 and also analysis of the electrochemical parameters deduced from the Nyquist plot and summarized in Table 3 are necessary. Various resistances are categorized as R_s , R_1 , R_2 , and R_3 , according to the equivalent circuit model of DSSCs defined in previous studies. The resistance at the interface of FTO/ TiO_2 , also called the “sheet resistance”, is denoted by R_s , while the charge transfer resistance at the interface of counter electrode/electrolyte is denoted by R_1 . Similarly, the charge transfer resistance at the interface of semiconductor/dye/electrolyte is denoted as R_2 , and the resistance to Nerst diffusion in the electrolyte is denoted by R_3 [64–67]. A DSSC device possessing a reduced sum of these internal resistances exhibits a good photovoltaic performance, as the charge transport mechanisms in DSSCs are influenced by these resistances [68]. It is also worth defining R_t here, which is the resistance to the transport of electrons in the mesoporous TiO_2 . However, for n-DSSCs, particularly under high illumination intensities, the value of R_t is very small and hence negligible [69]. Given that the FTO substrate along with the electrolyte used to fabricate the DSSCs were the same, R_s , R_1 , and R_3 must have similar values in the case of all the DSSCs, regardless of the various sensitizers utilized.

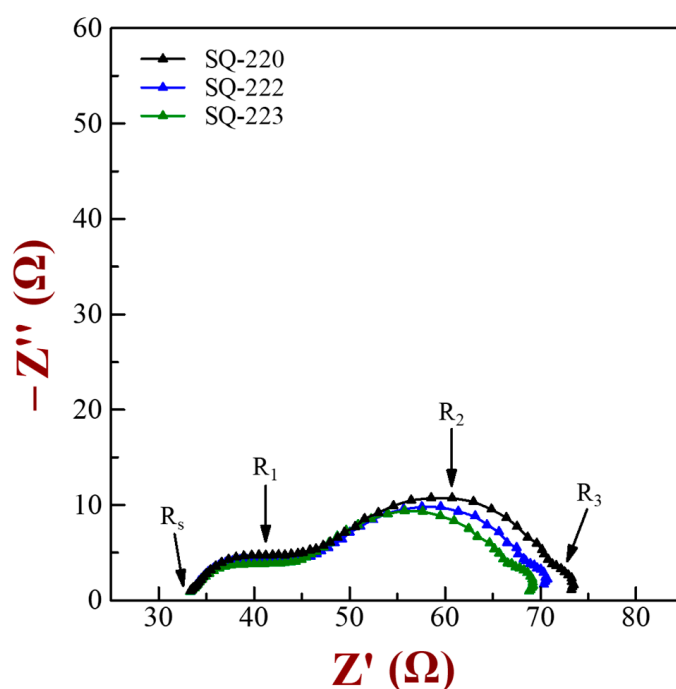


Figure 6. Nyquist plot for fabricated DSSCs using dyes SQ-220, SQ-222, and SQ-223 and I^-/I_3^- electrolyte.

Table 3. Electrochemical parameters for fabricated DSSCs with the respective dyes, SQ-220, SQ-222, SQ-223, and I^-/I_3^- redox electrolyte.

Sensitizing Dye	R_S (Ω)	R_1 (Ω)	R_2 (Ω)	R_3 (Ω)
SQ-220	33.32	12.52	25.39	2.02
SQ-222	33.30	12.07	23.07	1.92
SQ-223	33.28	12.17	21.09	2.26

As can be observed in Figure 6 and Table 3, the value of R_2 , the interfacial resistance associated with the process of charge transport at the interface of semiconductor/ TiO_2 /electrolyte, is different for DSSCs fabricated with different dyes, with SQ-220 exhibiting the highest value and SQ-223 exhibiting the lowest. The J_{sc} and V_{oc} of DSSCs are directly influenced by the charge recombination kinetics at the interface of TiO_2 /dye/electrolyte [70]. The V_{oc} of a DSSC is dependent on the difference between the electrolyte's (I^-/I_3^-) redox energy level and the TiO_2 's quasi-fermi level, and the shift in the TiO_2 's quasi-fermi level due to a shift in the conduction band edge of TiO_2 due to electron density fluctuation triggered by charge recombination at the interface of TiO_2 /dye/electrolyte directly affects the V_{oc} [71]. Earlier reports have defined R_2 as the resistance to charge recombination. In simple terms, it is the resistance to the movement of charges back towards the oxidized dye or the redox electrolyte [64]. Consequently, SQ-223 exhibits a lower V_{oc} because its resistance to charge recombination is lower as a result of lower R_2 values. SQ-220, with a higher value of R_2 , exhibits a higher value of V_{oc} . This difference in the value of R_2 can be mainly ascribed to the variation in the electron injection barrier value, which ultimately has a direct influence on charge injection. Therefore, the lower the electron injection, the lower the value of R_2 , hence the greater the recombination. Hence, along with dye aggregation, a lower electron injection barrier also affects the resistance to charge recombination, as SQ-223, with relatively lesser aggregation, shows a lower R_2 value. The cis-conformation of SQ-223, which usually prevents recombination by creating a hydrophobic layer with outwardly extending alkyl chains, could not lead to higher V_{oc} as a result of its lower electron injection barrier, i.e., low-lying LUMO energy level. We have earlier reported the dependence of V_{oc} on alkyl chain length, with a minimum chain length of four carbons giving a reasonable V_{oc} and the optimum V_{oc} achieved with an alkyl chain length of twelve carbons [63]. However, even when incorporating a shorter alkyl chain (butyl) on one of the indole donor moieties of the core-substituted unsymmetrical squaraine dyes, the V_{oc} values obtained were comparable to or somewhat better than those reported in the literature for core-substituted squaraine dyes with a similar molecular framework [40,41,72,73]. In addition to this, the J_{sc} of the DSSCs is also influenced by the charge recombination kinetics at the interface of TiO_2 /dye/electrolyte, as discussed earlier. The higher the value of R_2 , the more electrons are injected into the TiO_2 's CB. Similarly, the lower the value of R_2 , the fewer electrons are injected. As a result, SQ-220 with a higher value of R_2 should effectively prevent recombination, thus leading to more injection of electron into TiO_2 's CB, because of which it should ideally exhibit a higher J_{sc} value and SQ-223 should ideally exhibit a lower J_{sc} value. However, the opposite scenario is observed in this study. This is because of the fact that the photon-harvesting windows for the two dyes, SQ-220 and SQ-223, are totally different. SQ-223 exhibits wide-wavelength photon harvesting from 300 nm to 800 nm with an IPCE of 45% in the visible region and 68% in the far-red region, thus leading to a high J_{sc} value. In contrast, SQ-220 exhibits a narrow photon-harvesting window with practically no absorption in the visible region, because of which it exhibits a lower J_{sc} value.

4. Enhancement of PCE Employing Co-Sensitization Using Visible Dye

4.1. Optical Characterization

As SQ-223 absorbs light significantly in the solar spectrum's far-red to NIR region, a visible dye, D-131, with the molecular structure shown in Figure 7 along with SQ-223,

was used for co-adsorption with SQ-223 by making dye cocktails to have a complementary light absorption in both the visible and NIR wavelength regions of the solar spectrum. The best photovoltaic performance exhibited by SQ-223 amongst the dyes used in the current study also supported its selection for complementary light absorption. A closer analysis of the UV-visible spectra of D-131 and SQ-223, shown in Figure 8a, clearly shows that they exhibit complementary light absorption, indicating that these two dyes when co-adsorbed can lead to an improvement in the light absorption in the entire visible to NIR region. The electronic absorption spectra of the ethanolic solution of the dye cocktails made by taking various molar ratios of D-131 and SQ-223 are shown in Figure 8b. The dye cocktails' absorption spectra clearly display light absorption both in the 400–500 nm (visible region, due to D-131) and in the 550–700 nm (far-red region, due to SQ-223). The absorption spectra also lead us to the conclusion that the higher molar ratio of SQ-223 leads to a diminished light absorption associated with D-131, and also the absorption of light by D-131 is overlapping with the relatively small extent of the SQ-223's absorption in the visible region. The relatively lesser extent of light absorption by D-131 in the dye cocktail with a higher molar ratio of SQ-223 may be due to the lower ϵ value of D-131, thus necessitating the utilization of a greater fraction (molar ratio) of D-131 in the dye cocktail. Although the presence of a greater molar ratio of D-131 in the dye cocktail leads to a corresponding reduction in the SQ-223's light absorption, the higher ϵ value of SQ-223 leads to a greater light absorption even when it is present in a lower fraction.

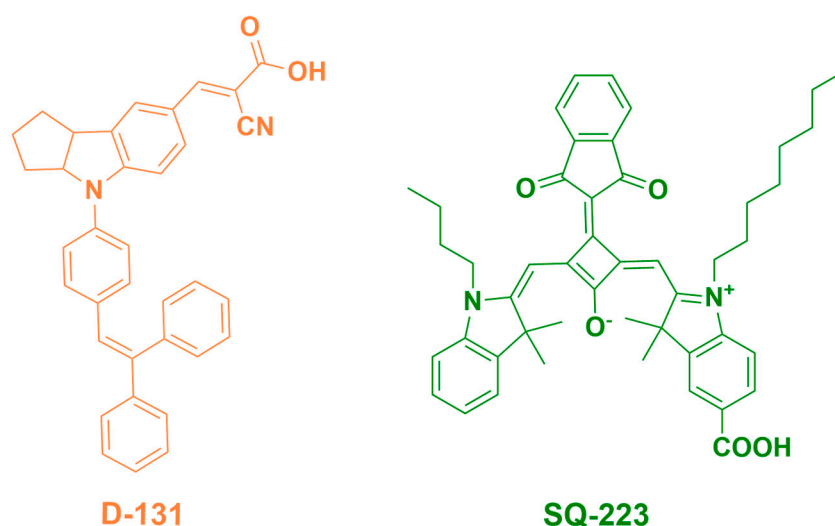


Figure 7. Molecular structure of D-131 (visible dye) and SQ-223 (unsymmetrical squaraine dye) utilized in this study.

4.2. Photovoltaic Characterization

The complementary photon harvesting exhibited by D-131 and SQ-223 in the visible and NIR wavelength regions, respectively, encouraged their use as a sensitizer in DSSCs with the aim of synergistic harvesting of photons in a broader wavelength region. The DSSCs were fabricated employing I^-/I_3^- redox electrolyte and utilizing individual dyes, D-131 and SQ-223, and also their cocktails in the molar ratios of 9:1 and 1:9 as sensitizers. The photocurrent action spectra, or the plot of incident photon to current conversion efficiency (IPCE) as a function of wavelength following illumination with monochromatic light, are depicted in Figure 9, along with the photovoltaic characteristics of DSSCs fabricated using individual dyes, D-131 and SQ-223, and their dye cocktails. The summary of photovoltaic parameters of the fabricated DSSCs, including J_{sc} , V_{oc} , FF, and overall PCE (%), are given in Table 4.

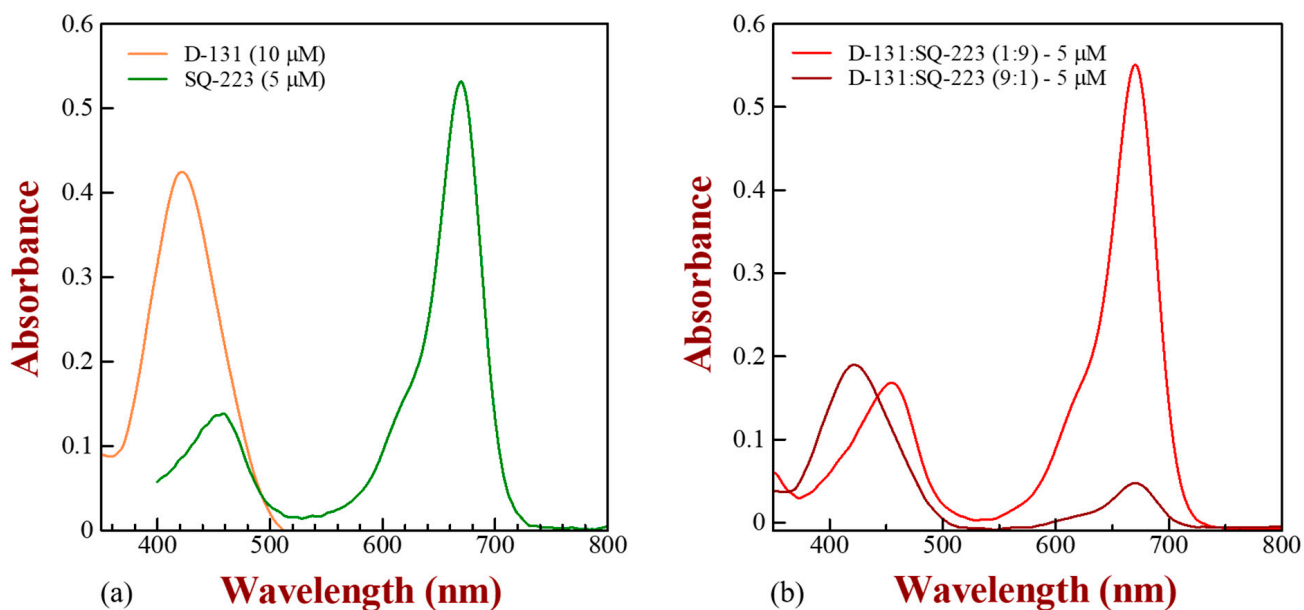


Figure 8. Electronic absorption spectra of ethanolic solutions of (a) D-131 (10 μM) and SQ-223 (5 μM), and (b) ethanolic solution of D-131 and SQ-223 dye cocktails in different molar ratios.

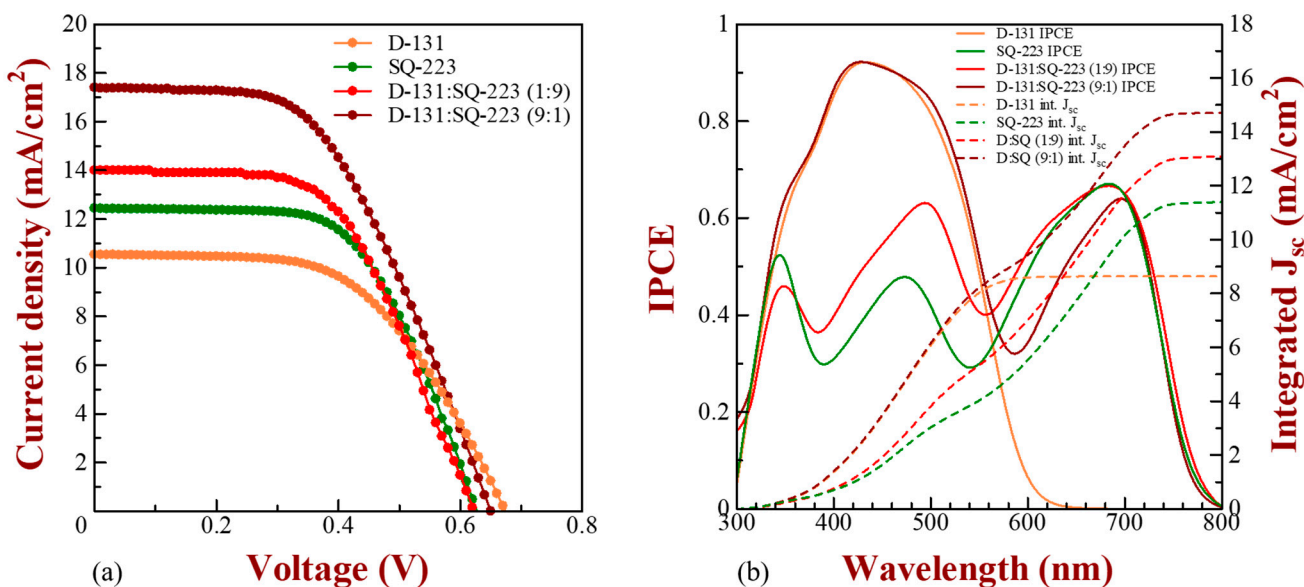


Figure 9. (a) Photovoltaic characteristics of fabricated DSSCs utilizing dyes, D-131 and SQ-223, and their dye cocktails in the molar ratios of (9:1) and (1:9) under simulated solar irradiation of 100 mW cm⁻², and (b) Photocurrent action spectra for the same DSSCs after monochromatic illumination.

Table 4. Photovoltaic parameters deduced after photovoltaic characterizations of fabricated DSSCs.

Sensitizing Dye	J_{sc} [mA/cm ²]	Integrated J_{sc} [mA/cm ²] (% Deviation)	V_{oc} [V]	FF	PCE [%]
D-131	10.54 (10.30 ± 0.23)	8.64 (18.02)	0.68 (0.68 ± 0.01)	0.55 (0.56 ± 0.01)	3.94 (3.81 ± 0.20)
SQ-223	12.44 (11.93 ± 0.46)	11.40 (8.36)	0.63 (0.62 ± 0.01)	0.60 (0.60 ± 0.01)	4.67 (4.42 ± 0.18)
D-131: SQ-223 (1:9)	14.01 (13.48 ± 0.38)	13.08 (6.64)	0.63 (0.63 ± 0.01)	0.56 (0.57 ± 0.01)	4.93 (4.79 ± 0.17)
D-131: SQ-223 (9:1)	17.40 (16.92 ± 0.47)	14.71 (15.46)	0.66 (0.64 ± 0.01)	0.51 (0.52 ± 0.01)	5.81 (5.59 ± 0.18)

The mean values of different parameters of four individual DSSCs are presented in parentheses along with their standard deviations. The values shown above the parentheses in each case demonstrate the best cell parameters.

The photocurrent action spectra of D-131 and SQ-223 are shown in Figure 9b, and it is clear that the two dyes display complementary harvesting of photons in the visible and far-red regions, resulting in wide-wavelength photon harvesting (400–800 nm). The complementary nature of the two dyes can also be ascertained by the fact that the lower V_{oc} of SQ-223 has been substantially enhanced on its co-adsorption with D-131, as shown in Table 4. Additionally, the IPCE of the dye cocktail in the molar ratio (9:1) demonstrates that the addition of SQ-223 significantly improves harvesting of photons in the solar spectrum's far-red region, which was typically missing in D-131. The photocurrent action spectrum for the dye cocktail in the molar ratio (1:9) demonstrates that visible photon harvesting is relatively enhanced in comparison to the individual dye, SQ-223. This is true even though SQ-223 itself exhibited a relatively less intense visible light absorption. However, due to the large difference in the molar extinction coefficients of the two dyes, the photon harvesting in the visible region (due to D-131) is not substantial and this suggests the use of D-131 in a higher molar ratio. The dye loading amounts after using the visible dye D-131 in the higher ratio in the dye cocktail (9:1) have been summarized in Table S2 (see supplementary material). The results exhibit dye loading precisely in the 9:1 ratio.

The dye cocktail of D-131 and SQ-223 in the ratio (1:9) exhibits photon harvesting in both the visible and the far-red region, and also exhibits a reasonable improvement in overall PCE (4.93%), when compared to the overall PCE (3.94%) of D-131; however, there was not much improvement in the overall PCE (4.93%) when compared with the overall PCE (4.67%) of SQ-223. Even after the co-adsorption of both the dyes, the overall PCE improved only slightly. This can be explained by the fact that D-131 has relatively poor photon harvesting of 62% compared to its individual photon harvesting of 92%. It is worth noting that the lower ϵ value of D-131 suggests that a higher molar fraction of D-131 should be added to the dye cocktail, as more molecules are required for a dye with a lower ϵ value to harvest photons sufficiently. This observation is supported by the finding that when the molar ratio of D-131 was increased from 1:9 to 9:1 in the dye cocktail, D-131 displayed a photon harvesting of 92% in the visible region in combination with a photon harvesting of 66% by the dye SQ-223 in the far-red to NIR region. Consequently, using a cocktail of D-131 and SQ-223 in a 9:1 molar ratio resulted in a maximum harvesting of photons both in the visible (D-131) and the far-red to NIR regions (SQ-223), leading to an increased J_{sc} of 17.40 mA/cm², an increased V_{oc} of 0.66 V, and an FF of 0.51, thus yielding an overall PCE of 5.81% which is significantly greater than the PCE exhibited by the individual dyes D-131 (3.94%) and SQ-223 (4.67%). Another interesting observation to be noted here is that a substantial increase in the J_{sc} (17.40 mA/cm²) was observed when compared with the individual J_{sc} of D-131 (10.54 mA/cm²) and SQ-223 (12.44 mA/cm²). The complementary photon harvesting exhibited by the dyes in the visible (D-131) and NIR (SQ-223) regions, thus resulting in a panchromatic photon harvesting in the region between 300 nm to 800 nm,

is what causes the significant increase in the J_{sc} of the DSSC fabricated using a dye cocktail of D-131 and SQ-223 in a 9:1 molar ratio.

5. Conclusions

Three squaric acid core substituted unsymmetrical squaraine sensitizers, SQ-220, SQ-222, and SQ-223, were computationally designed, synthesized, and utilized as sensitizers in DSSCs. In addition to causing a red shift in the λ_{max} , the incorporation of electron acceptors in the cyclobutene ring at the center also resulted in a lowering of the dye's HOMO level, which therefore made dye regeneration easy. In addition to this, the presence of electron acceptors resulted in the emergence of a secondary high-energy absorption band within the visible spectrum, thus facilitating wide-wavelength photon harvesting. SQ-223 exhibited the best photovoltaic performance as a result of its wide-wavelength photon harvesting, a result of its significant visible light absorption and low-lying HOMO level. As a consequence of their complementary light absorption, SQ-223 and a visible dye, D-131, were employed to co-sensitize mesoporous TiO_2 . The results of the investigation into the photovoltaic performance of the D-131 and SQ-223 co-sensitized DSSCs in various molar ratios led to the conclusion that dye cocktails in the molar ratio of 9:1 gave the best photovoltaic results, showing a significantly increased J_{sc} of 17.40 mA/cm^2 , V_{oc} of 0.66 V , and FF of 0.51 , ultimately yielding an overall PCE of 5.81% , in comparison to their individual performance and their performance in the dye cocktail ratio of (1:9). Hence, this study encourages further design of novel far-red to NIR-sensitive sensitizers for DSSC applications, considering the importance of wide-wavelength photon harvesting and lower HOMO energy level.

Supplementary Materials: The following supporting information can be downloaded at: <https://www.mdpi.com/article/10.3390/colorants2040034/s1>, Scheme S1: Synthetic details, along with FAB-MS, HR-FAB-MS, ^1H NMR, and ^{13}C NMR characterizations; Figure S1: Theoretical absorption spectra; Figure S2: Cyclic Voltammetry; Figure S3: Schematics showing calculation of sensitizer's potential shift with respect to that of ferrocene; Figure S4: Dye loading; Figure S5: Calibration curves for dye loading; Table S1: Theoretically calculated absorption parameters; and Table S2: Dye loading. References [47,53] are cited in the Supplementary Materials.

Author Contributions: Conceptualization, S.P. and S.S.P.; methodology, S.P.; Software, S.P. and S.S.P.; validation, S.P.; formal analysis, S.P. and S.S.; investigation, S.P. and Y.K.; data curation, S.P. and Y.K.; writing—original draft preparation, S.P.; writing—review and editing, S.P. and S.S.P.; visualization, S.P.; supervision, S.S.P. All authors have read and agreed to the published version of the manuscript.

Funding: This research received no external funding.

Institutional Review Board Statement: Not applicable.

Informed Consent Statement: Not applicable.

Data Availability Statement: The data can be made available on request.

Conflicts of Interest: The authors declare no conflict of interest.

References

1. Kokkonen, M.; Talebi, P.; Zhou, J.; Asgari, S.; Soomro, S.A.; Elsehrawy, F.; Halme, J.; Ahmad, S.; Hagfeldt, A.; Hashmi, S.G. Advanced Research Trends in Dye-Sensitized Solar Cells. *J. Mater. Chem. A* **2021**, *9*, 10527–10545. [[CrossRef](#)] [[PubMed](#)]
2. Shahid, M.U.; Mohamed, N.M.; Muhsan, A.S.; Zaine, S.N.A.; Bashiri, R.; Khatani, M.; Samsudin, A.E. Solvent Exfoliated Graphene Incorporated Mixed Phase TiO_2 Transparent Photoelectrode for the Efficient and Color Transparent Dye-Sensitized Solar Cell. *Sol. Energy* **2020**, *206*, 317–329. [[CrossRef](#)]
3. Yu, M.; McCulloch, W.D.; Beauchamp, D.R.; Huang, Z.; Ren, X.; Wu, Y. Aqueous Lithium–Iodine Solar Flow Battery for the Simultaneous Conversion and Storage of Solar Energy. *J. Am. Chem. Soc.* **2015**, *137*, 8332–8335. [[CrossRef](#)] [[PubMed](#)]
4. Roy, P.; Kumar Sinha, N.; Tiwari, S.; Khare, A. A Review on Perovskite Solar Cells: Evolution of Architecture, Fabrication Techniques, Commercialization Issues and Status. *Sol Energy* **2020**, *198*, 665–688. [[CrossRef](#)]
5. Freitag, M.; Teuscher, J.; Saygili, Y.; Zhang, X.; Giordano, F.; Liska, P.; Hua, J.; Zakeeruddin, S.M.; Moser, J.-E.; Grätzel, M.; et al. Dye-Sensitized Solar Cells for Efficient Power Generation under Ambient Lighting. *Nat. Photonics* **2017**, *11*, 372–378. [[CrossRef](#)]

6. O'Regan, B.; Grätzel, M. A Low-Cost, High-Efficiency Solar Cell Based on Dye-Sensitized Colloidal TiO₂ Films. *Nature* **1991**, *353*, 737–740. [[CrossRef](#)]
7. Hug, H.; Bader, M.; Mair, P.; Glatzel, T. Biophotovoltaics: Natural Pigments in Dye-Sensitized Solar Cells. *Appl. Energy* **2014**, *115*, 216–225. [[CrossRef](#)]
8. Amogne, N.Y.; Ayele, D.W.; Tsigie, Y.A. Recent Advances in Anthocyanin Dyes Extracted from Plants for Dye Sensitized Solar Cell. *Mater. Renew. Sustain. Energy* **2020**, *9*, 23. [[CrossRef](#)]
9. Gu, P.; Yang, D.; Zhu, X.; Sun, H.; Li, J. Fabrication and Characterization of Dye-Sensitized Solar Cells Based on Natural Plants. *Chem. Phys. Lett.* **2018**, *693*, 16–22. [[CrossRef](#)]
10. Mátravölgyi, B.; Hergert, T.; Thurner, A.; Varga, B.; Sangiorgi, N.; Bondoni, R.; Zani, L.; Reginato, G.; Calamante, M.; Sinicropi, A.; et al. Synthesis and Investigation of Solar-Cell Photosensitizers Having a Fluorazone Backbone. *Eur. J. Org. Chem.* **2017**, *2017*, 1843–1854. [[CrossRef](#)]
11. Sangiorgi, N.; Sangiorgi, A.; Dessì, A.; Zani, L.; Calamante, M.; Reginato, G.; Mordini, A.; Sanson, A. Improving the Efficiency of Thin-Film Fiber-Shaped Dye-Sensitized Solar Cells by Using Organic Sensitizers. *Sol. Energy Mater. Sol. Cells* **2020**, *204*, 110209. [[CrossRef](#)]
12. Grätzel, M. Conversion of Sunlight to Electric Power by Nanocrystalline Dye-Sensitized Solar Cells*1. *J. Photochem. Photobiol. A Chem.* **2004**, *164*, 3–14. [[CrossRef](#)]
13. Tachibana, Y.; Moser, J.E.; Grätzel, M.; Klug, D.R.; Durrant, J.R. Subpicosecond Interfacial Charge Separation in Dye-Sensitized Nanocrystalline Titanium Dioxide Films. *J. Phys. Chem.* **1996**, *100*, 20056–20062. [[CrossRef](#)]
14. Pradhan, A.; Morimoto, T.; Saikiran, M.; Kapil, G.; Hayase, S.; Pandey, S.S. Investigation of the Minimum Driving Force for Dye Regeneration Utilizing Model Squaraine Dyes for Dye-Sensitized Solar Cells. *J. Mater. Chem. A* **2017**, *5*, 22672–22682. [[CrossRef](#)]
15. Zhang, L.; Yang, X.; Wang, W.; Gurzadyan, G.G.; Li, J.; Li, X.; An, J.; Yu, Z.; Wang, H.; Cai, B.; et al. 13.6% Efficient Organic Dye-Sensitized Solar Cells by Minimizing Energy Losses of the Excited State. *ACS Energy Lett.* **2019**, *4*, 943–951. [[CrossRef](#)]
16. Yao, Z.; Zhang, M.; Wu, H.; Yang, L.; Li, R.; Wang, P. Donor/Acceptor Indenoperylene Dye for Highly Efficient Organic Dye-Sensitized Solar Cells. *J. Am. Chem. Soc.* **2015**, *137*, 3799–3802. [[CrossRef](#)]
17. Nazeeruddin, M.K.; Kay, A.; Rodicio, I.; Humphry-Baker, R.; Mueller, E.; Liska, P.; Vlachopoulos, N.; Graetzel, M. Conversion of Light to Electricity by Cis-X₂bis(2,2'-Bipyridyl-4,4'-Dicarboxylate)Ruthenium(II) Charge-Transfer Sensitizers (X = Cl-, Br-, I-, CN-, and SCN-) on Nanocrystalline Titanium Dioxide Electrodes. *J. Am. Chem. Soc.* **1993**, *115*, 6382–6390. [[CrossRef](#)]
18. Nazeeruddin, M.K.; Péchy, P.; Renouard, T.; Zakeeruddin, S.M.; Humphry-Baker, R.; Comte, P.; Liska, P.; Cevey, L.; Costa, E.; Shklover, V.; et al. Engineering of Efficient Panchromatic Sensitizers for Nanocrystalline TiO₂-Based Solar Cells. *J. Am. Chem. Soc.* **2001**, *123*, 1613–1624. [[CrossRef](#)]
19. Yella, A.; Lee, H.-W.; Tsao, H.N.; Yi, C.; Chandiran, A.K.; Nazeeruddin, M.K.; Diau, E.W.-G.; Yeh, C.-Y.; Zakeeruddin, S.M.; Grätzel, M. Porphyrin-Sensitized Solar Cells with Cobalt (II/III)-Based Redox Electrolyte Exceed 12 Percent Efficiency. *Science* **2011**, *334*, 629–634. [[CrossRef](#)]
20. Liang, M.; Chen, J. Arylamine Organic Dyes for Dye-Sensitized Solar Cells. *Chem. Soc. Rev.* **2013**, *42*, 3453. [[CrossRef](#)]
21. Mishra, A.; Fischer, M.K.R.; Bäuerle, P. Metal-Free Organic Dyes for Dye-Sensitized Solar Cells: From Structure: Property Relationships to Design Rules. *Angew. Chem. Int. Ed.* **2009**, *48*, 2474–2499. [[CrossRef](#)] [[PubMed](#)]
22. Grisorio, R.; De Marco, L.; Baldisserrri, C.; Martina, F.; Serantoni, M.; Gigli, G.; Suranna, G.P. Sustainability of Organic Dye-Sensitized Solar Cells: The Role of Chemical Synthesis. *ACS Sustain. Chem. Eng.* **2015**, *3*, 770–777. [[CrossRef](#)]
23. Cid, J.-J.; Yum, J.-H.; Jang, S.-R.; Nazeeruddin, M.K.; Martínez-Ferrero, E.; Palomares, E.; Ko, J.; Grätzel, M.; Torres, T. Molecular Cosensitization for Efficient Panchromatic Dye-Sensitized Solar Cells. *Angew. Chem. Int. Ed.* **2007**, *46*, 8358–8362. [[CrossRef](#)] [[PubMed](#)]
24. Reddy, P.Y.; Giribabu, L.; Lyness, C.; Snaith, H.J.; Vijaykumar, C.; Chandrasekharam, M.; Lakshmikantam, M.; Yum, J.-H.; Kalyanasundaram, K.; Grätzel, M.; et al. Efficient Sensitization of Nanocrystalline TiO₂ Films by a Near-IR-Absorbing Unsymmetrical Zinc Phthalocyanine. *Angew. Chem. Int. Ed.* **2007**, *46*, 373–376. [[CrossRef](#)] [[PubMed](#)]
25. Higashino, T.; Kawamoto, K.; Sugiura, K.; Fujimori, Y.; Tsuji, Y.; Kurotobi, K.; Ito, S.; Imahori, H. Effects of Bulky Substituents of Push–Pull Porphyrins on Photovoltaic Properties of Dye-Sensitized Solar Cells. *ACS Appl. Mater. Interfaces* **2016**, *8*, 15379–15390. [[CrossRef](#)]
26. Tang, Y.; Wang, Y.; Li, X.; Ågren, H.; Zhu, W.-H.; Xie, Y. Porphyrins Containing a Triphenylamine Donor and up to Eight Alkoxy Chains for Dye-Sensitized Solar Cells: A High Efficiency of 10.9%. *ACS Appl. Mater. Interfaces* **2015**, *7*, 27976–27985. [[CrossRef](#)]
27. Saccone, D.; Galliano, S.; Barbero, N.; Quagliotto, P.; Viscardi, G.; Barolo, C. Polymethine Dyes in Hybrid Photovoltaics: Structure-Properties Relationships. *Eur. J. Org. Chem.* **2016**, *2016*, 2244–2259. [[CrossRef](#)]
28. Pandey, S.S.; Watanabe, R.; Fujikawa, N.; Shivashimpi, G.M.; Ogomi, Y.; Yamaguchi, Y.; Hayase, S. Effect of Extended π -Conjugation on Photovoltaic Performance of Dye Sensitized Solar Cells Based on Unsymmetrical Squaraine Dyes. *Tetrahedron* **2013**, *69*, 2633–2639. [[CrossRef](#)]
29. Ajayaghosh, A. Chemistry of Squaraine-Derived Materials: Near-IR Dyes, Low Band Gap Systems, and Cation Sensors. *Acc. Chem. Res.* **2005**, *38*, 449–459. [[CrossRef](#)]
30. Sreejith, S.; Carol, P.; Chithra, P.; Ajayaghosh, A. Squaraine Dyes: A Mine of Molecular Materials. *J. Mater. Chem.* **2008**, *18*, 264–274. [[CrossRef](#)]

31. Yang, D.; Sano, T.; Sasabe, H.; Kido, J. A Novel π -D1-A-D2 Type Low Bandgap Squaraine Dye for Efficient Small Molecular Organic Solar Cells. *Dye. Pigment.* **2019**, *163*, 564–572. [[CrossRef](#)]
32. Treibs, A.; Jacob, K. Cyclotrimethine Dyes Derived from Squaric Acid. *Angew. Chem. Int. Ed.* **1965**, *4*, 694. [[CrossRef](#)]
33. Wu, Y.; Zhu, W. Organic Sensitizers from D- π -A to D-A- π -A: Effect of the Internal Electron-Withdrawing Units on Molecular Absorption, Energy Levels and Photovoltaic Performances. *Chem. Soc. Rev.* **2013**, *42*, 2039–2058. [[CrossRef](#)] [[PubMed](#)]
34. Griffiths, J.; Park, S. Facile Preparative Redox Chemistry of Bis(4-Dialkylaminophenyl)Squaraine Dyes. *Tetrahedron Lett.* **2002**, *43*, 7669–7671. [[CrossRef](#)]
35. Pandey, S.S.; Morimoto, T.; Fujikawa, N.; Hayase, S. Combined Theoretical and Experimental Approaches for Development of Squaraine Dyes with Small Energy Barrier for Electron Injection. *Sol. Energy Mater. Sol. Cells* **2017**, *159*, 625–632. [[CrossRef](#)]
36. Frisch, M.J.; Trucks, G.W.; Schlegel, H.B.; Scuseria, G.E.; Robb, M.A.; Cheeseman, J.R.; Scalmani, G.; Barone, V.; Petersson, G.A.; Nakatsuji, H.; et al. *G16_C01 2016*; Gaussian 16, Revision A.03; Gaussian, Inc.: Wallingford, CT, USA, 2016.
37. Improta, R.; Barone, V.; Scalmani, G.; Frisch, M.J. A State-Specific Polarizable Continuum Model Time Dependent Density Functional Theory Method for Excited State Calculations in Solution. *J. Chem. Phys.* **2006**, *125*, 054103. [[CrossRef](#)]
38. Beverina, L.; Ruffo, R.; Mari, C.M.; Pagani, G.A.; Sassi, M.; De Angelis, F.; Fantacci, S.; Yum, J.-H.; Grätzel, M.; Nazeeruddin, M.K. Panchromatic Cross-Substituted Squaraines for Dye-Sensitized Solar Cell Applications. *ChemSusChem* **2009**, *2*, 621–624. [[CrossRef](#)]
39. Mayerhöffer, U.; Fimmel, B.; Würthner, F. Bright Near-Infrared Fluorophores Based on Squaraines by Unexpected Halogen Effects. *Angew. Chem. Int. Ed.* **2012**, *51*, 164–167. [[CrossRef](#)]
40. Qin, C.; Numata, Y.; Zhang, S.; Yang, X.; Islam, A.; Zhang, K.; Chen, H.; Han, L. Novel Near-Infrared Squaraine Sensitizers for Stable and Efficient Dye-Sensitized Solar Cells. *Adv. Funct. Mater.* **2014**, *24*, 3059–3066. [[CrossRef](#)]
41. Galliano, S.; Novelli, V.; Barbero, N.; Smarra, A.; Viscardi, G.; Borrelli, R.; Sauvage, F.; Barolo, C. Dicyanovinyl and Cyano-Ester Benzoinolenine Squaraine Dyes: The Effect of the Central Functionalization on Dye-Sensitized Solar Cell Performance. *Energies* **2016**, *9*, 486. [[CrossRef](#)]
42. Paternò, G.M.; Barbero, N.; Galliano, S.; Barolo, C.; Lanzani, G.; Scotognella, F.; Borrelli, R. Excited State Photophysics of Squaraine Dyes for Photovoltaic Applications: An Alternative Deactivation Scenario. *J. Mater. Chem. C* **2018**, *6*, 2778–2785. [[CrossRef](#)]
43. Kulinich, A.V.; Derevyanko, N.A.; Mikitenko, E.K.; Ishchenko, A.A. Merocyanines Based on 1,3-Indanedione: Electronic Structure and Solvatochromism. *J. Phys. Org. Chem.* **2011**, *24*, 732–742. [[CrossRef](#)]
44. Pigot, C.; Peralta, S.; Bui, T.-T.; Nechab, M.; Dumur, F. Push-Pull Dyes Based on Michler’s Aldehyde: Design and Characterization of the Optical and Electrochemical Properties. *Dye Pigment.* **2022**, *202*, 110278. [[CrossRef](#)]
45. Barcenas, G.; Biaggne, A.; Mass, O.A.; Wilson, C.K.; Obukhova, O.M.; Kolosova, O.S.; Tatarets, A.L.; Terpetschnig, E.; Pensack, R.D.; Lee, J.; et al. First-Principles Studies of Substituent Effects on Squaraine Dyes. *RSC Adv.* **2021**, *11*, 19029–19040. [[CrossRef](#)]
46. Cole, J.M.; Pepe, G.; Al Bahri, O.K.; Cooper, C.B. Cosensitization in Dye-Sensitized Solar Cells. *Chem. Rev.* **2019**, *119*, 7279–7327. [[CrossRef](#)]
47. Su, B.; Girault, H.H. Absolute Standard Redox Potential of Monolayer-Protected Gold Nanoclusters. *J. Phys. Chem. B* **2005**, *109*, 11427–11431. [[CrossRef](#)]
48. Mosconi, E.; Yum, J.-H.; Kessler, F.; Gómez García, C.J.; Zuccaccia, C.; Cinti, A.; Nazeeruddin, M.K.; Grätzel, M.; De Angelis, F. Cobalt Electrolyte/Dye Interactions in Dye-Sensitized Solar Cells: A Combined Computational and Experimental Study. *J. Am. Chem. Soc.* **2012**, *134*, 19438–19453. [[CrossRef](#)]
49. Geiger, T.; Kuster, S.; Yum, J.-H.; Moon, S.-J.; Nazeeruddin, M.K.; Grätzel, M.; Nüesch, F. Molecular Design of Unsymmetrical Squaraine Dyes for High Efficiency Conversion of Low Energy Photons into Electrons Using TiO₂ Nanocrystalline Films. *Adv. Funct. Mater.* **2009**, *19*, 2720–2727. [[CrossRef](#)]
50. Anthonysamy, A.; Lee, Y.; Karunakaran, B.; Ganapathy, V.; Rhee, S.-W.; Karthikeyan, S.; Kim, K.S.; Ko, M.J.; Park, N.-G.; Ju, M.-J.; et al. Molecular Design and Synthesis of Ruthenium(II) Sensitizers for Highly Efficient Dye-Sensitized Solar Cells. *J. Mater. Chem.* **2011**, *21*, 12389–12397. [[CrossRef](#)]
51. Chen, G.; Sasabe, H.; Igarashi, T.; Hong, Z.; Kido, J. Squaraine Dyes for Organic Photovoltaic Cells. *J. Mater. Chem. A* **2015**, *3*, 14517–14534. [[CrossRef](#)]
52. Eisfeld, A.; Briggs, J.S. The J- and H-Bands of Organic Dye Aggregates. *Chem. Phys.* **2006**, *324*, 376–384. [[CrossRef](#)]
53. Yum, J.-H.; Walter, P.; Huber, S.; Rentsch, D.; Geiger, T.; Nüesch, F.; De Angelis, F.; Grätzel, M.; Nazeeruddin, M.K. Efficient Far Red Sensitization of Nanocrystalline TiO₂ Films by an Unsymmetrical Squaraine Dye. *J. Am. Chem. Soc.* **2007**, *129*, 10320–10321. [[CrossRef](#)] [[PubMed](#)]
54. Unger, E.L.; Morandeira, A.; Persson, M.; Zietz, B.; Ripaud, E.; Leriche, P.; Roncali, J.; Hagfeldt, A.; Boschloo, G. Contribution from a Hole-Conducting Dye to the Photocurrent in Solid-State Dye-Sensitized Solar Cells. *Phys. Chem. Chem. Phys.* **2011**, *13*, 20172–20177. [[CrossRef](#)]
55. Zhang, L.; Cole, J.M. Dye Aggregation in Dye-Sensitized Solar Cells. *J. Mater. Chem. A* **2017**, *5*, 19541–19559. [[CrossRef](#)]
56. Yum, J.H.; Moon, S.J.; Humphry-Baker, R.; Walter, P.; Geiger, T.; Nüesch, F.; Grätzel, M.; Nazeeruddin, M.D.K. Effect of Coadsorbent on the Photovoltaic Performance of Squaraine Sensitized Nanocrystalline Solar Cells. *Nanotechnology* **2008**, *19*, 424005. [[CrossRef](#)] [[PubMed](#)]

57. Lim, J.M.; Yoon, Z.S.; Shin, J.-Y.; Kim, K.S.; Yoon, M.-C.; Kim, D. The Photophysical Properties of Expanded Porphyrins: Relationships between Aromaticity, Molecular Geometry and Non-Linear Optical Properties. *Chem. Commun.* **2008**, *45*, 261–273. [[CrossRef](#)]
58. Ogomi, Y.; Kato, T.; Hayase, S. Dye Sensitized Solar Cells Consisting of Ionic Liquid and Solidification. *J. Photopolym. Sci. Technol.* **2006**, *19*, 403–408. [[CrossRef](#)]
59. Hagfeldt, A.; Graetzel, M. Light-Induced Redox Reactions in Nanocrystalline Systems. *Chem. Rev.* **1995**, *95*, 49–68. [[CrossRef](#)]
60. Yao, Z.; Guo, Y.; Wang, L.; Hao, Y.; Guo, Y.; Franchi, D.; Zhang, F.; Kloo, L.; Sun, L. Energy-Loss Reduction as a Strategy to Improve the Efficiency of Dye-Sensitized Solar Cells. *Sol. RRL* **2019**, *3*, 1900253. [[CrossRef](#)]
61. Pastore, M.; Fantacci, S.; De Angelis, F. Modeling Excited States and Alignment of Energy Levels in Dye-Sensitized Solar Cells: Successes, Failures, and Challenges. *J. Phys. Chem. C* **2013**, *117*, 3685–3700. [[CrossRef](#)]
62. Nazeeruddin, M.K.; De Angelis, F.; Fantacci, S.; Selloni, A.; Viscardi, G.; Liska, P.; Ito, S.; Takeru, B.; Grätzel, M. Combined Experimental and DFT-TDDFT Computational Study of Photoelectrochemical Cell Ruthenium Sensitizers. *J. Am. Chem. Soc.* **2005**, *127*, 16835–16847. [[CrossRef](#)] [[PubMed](#)]
63. Pandey, S.S.; Inoue, T.; Fujikawa, N.; Yamaguchi, Y.; Hayase, S. Substituent Effect in Direct Ring Functionalized Squaraine Dyes on near Infra-Red Sensitization of Nanocrystalline TiO₂ for Molecular Photovoltaics. *J. Photochem. Photobiol. A Chem.* **2010**, *214*, 269–275. [[CrossRef](#)]
64. Hoshikawa, T.; Yamada, M.; Kikuchi, R.; Eguchi, K. Impedance Analysis of Internal Resistance Affecting the Photoelectrochemical Performance of Dye-Sensitized Solar Cells. *J. Electrochem. Soc.* **2005**, *152*, E68. [[CrossRef](#)]
65. Kapil, G.; Ohara, J.; Ogomi, Y.; Pandey, S.S.; Ma, T.; Hayase, S. Fabrication and Characterization of Coil Type Transparent Conductive Oxide-Less Cylindrical Dye-Sensitized Solar Cells. *RSC Adv.* **2014**, *4*, 22959–22963. [[CrossRef](#)]
66. Zhang, Y.; Sun, Z.; Cheng, S.; Yan, F. Plasmon-Induced Broadband Light-Harvesting for Dye-Sensitized Solar Cells Using a Mixture of Gold Nanocrystals. *ChemSusChem* **2016**, *9*, 813–819. [[CrossRef](#)] [[PubMed](#)]
67. Huo, J.; Wu, J.; Zheng, M.; Tu, Y.; Lan, Z. A Transparent Cobalt Sulfide/Reduced Graphene Oxide Nanostructure Counter Electrode for High Efficient Dye-Sensitized Solar Cells. *Electrochim. Acta* **2016**, *187*, 210–217. [[CrossRef](#)]
68. Hwang, D.-K.; Lee, B.; Kim, D.-H. Efficiency Enhancement in Solid Dye-Sensitized Solar Cell by Three-Dimensional Photonic Crystal. *RSC Adv.* **2013**, *3*, 3017. [[CrossRef](#)]
69. Fabregat-Santiago, F.; Bisquert, J.; Palomares, E.; Otero, L.; Kuang, D.; Zakeeruddin, S.M.; Grätzel, M. Correlation between Photovoltaic Performance and Impedance Spectroscopy of Dye-Sensitized Solar Cells Based on Ionic Liquids. *J. Phys. Chem. C* **2007**, *111*, 6550–6560. [[CrossRef](#)]
70. Yella, A.; Humphry-Baker, R.; Curchod, B.F.E.; Ashari Astani, N.; Teuscher, J.; Polander, L.E.; Mathew, S.; Moser, J.-E.; Tavernelli, I.; Rothlisberger, U.; et al. Molecular Engineering of a Fluorene Donor for Dye-Sensitized Solar Cells. *Chem. Mater.* **2013**, *25*, 2733–2739. [[CrossRef](#)]
71. Karjule, N.; Munavvar Fairoos, M.K.; Nithyanandhan, J. Heterotriangulene-Based Unsymmetrical Squaraine Dyes: Synergistic Effects of Donor Moieties and out-of-Plane Branched Alkyl Chains on Dye Cell Performance. *J. Mater. Chem. A* **2016**, *4*, 18910–18921. [[CrossRef](#)]
72. Zhang, K.; Qin, C.; Yang, X.; Islam, A.; Zhang, S.; Chen, H.; Han, L. High-Performance, Transparent, Dye-Sensitized Solar Cells for See-Through Photovoltaic Windows. *Adv. Energy Mater.* **2014**, *4*, 1301966. [[CrossRef](#)]
73. Punitharasu, V.; Mele Kavungathodi, M.F.; Singh, A.K.; Nithyanandhan, J. π -Extended Cis—Configured Unsymmetrical Squaraine Dyes for Dye-Sensitized Solar Cells: Panchromatic Response. *ACS Appl. Energy Mater.* **2019**, *2*, 8464–8472. [[CrossRef](#)]

Disclaimer/Publisher’s Note: The statements, opinions and data contained in all publications are solely those of the individual author(s) and contributor(s) and not of MDPI and/or the editor(s). MDPI and/or the editor(s) disclaim responsibility for any injury to people or property resulting from any ideas, methods, instructions or products referred to in the content.